

Electrified synthesis of *n*-propanol using a dilute alloy catalyst

Received: 21 January 2024

Accepted: 28 January 2025

Published online: 28 February 2025

 Check for updates

Yuanjun Chen^{1,6}, Xinyue Wang^{1,2,6}, Xiao-Yan Li^{1,6}, Rui Kai Miao^{3,6}, Juncai Dong⁴, Zilin Zhao², Chuhao Liu⁵, Jianan Erick Huang¹, Jinhong Wu³, Senlin Chu², Weiyan Ni¹, Zunmin Guo³, Yi Xu³, Pengfei Ou¹, Bingjun Xu⁵, Yang Hou²✉, David Sinton³✉ & Edward H. Sargent¹✉

N-propanol is an important industrial solvent but the current industrial routes for its production rely on fossil fuels and generate high carbon dioxide emissions. Replacing fossil processes with electrochemical systems powered using renewable energy offers one route to reduce the carbon intensity of *n*-propanol manufacture. The electrosynthesis of *n*-propanol via carbon monoxide electroreduction relies on the coupling of C₁ and C₂ intermediates, and these are preferentially stabilized on different sites. Here we pursued the synthesis of catalysts in which a high-oxygen-affinity metal (such as Sn in the best catalysts herein) is present in dilute quantities within a Cu matrix. The Sn–Cu catalyst is then formed into a catalyst/carbon/ionomer heterojunction architecture that reverses electro-osmotic drag to concentrate the *n*-propanol produced. We achieve *n*-propanol electrosynthesis from carbon monoxide with a Faradaic efficiency of 47 ± 3% and a concentration of 30 wt% at an energy efficiency of 24%. We report stable *n*-propanol electrosynthesis for 120 h in a membrane-electrode assembly electrolyser.

The chemical sector accounts for 28% of total industrial energy demand^{1,2}. Today this demand is fulfilled principally using fossil fuels, leading to substantial carbon dioxide (CO₂) emissions³. *N*-propanol is an industrial solvent used in coatings, pigments, dyes, as a fuel additive and in paint, and is produced at a market volume of US\$3 billion a year⁴. In addition, *n*-propanol is readily dehydrated, under mild conditions, to propylene that is produced at US\$130 billion a year, and a precursor to polypropylene, propylene oxide (used in polyurethane) and acrylonitrile⁵.

Today *n*-propanol is produced via a two-step process: the hydroformylation of ethylene with carbon monoxide (CO) and hydrogen (H₂) at 20 MPa and roughly 80–150 °C to form propanal, followed by the hydrogenation of propanal with H₂ (refs. 6–9; Fig. 1a). Overall the

feedstocks and emissions lead to more than 4 tonnes of CO₂-equivalent per tonne of *n*-propanol produced¹⁰.

Electrosynthesis of *n*-propanol powered using low-carbon electricity (Fig. 1b) could consume CO₂ (such as that captured from air) and substantially decarbonize the process^{11–13}. The direct electrosynthesis of *n*-propanol from CO₂ electroreduction (CO₂R) suffers from limited energy efficiency and also from CO₂ loss; the latter arises from carbonate and/or bicarbonate formation and requires an additional CO₂ regeneration step that is energy intensive^{12–15}.

Motivated by the increasing availability of CO as a feedstock from electrochemical CO₂ to CO conversion technologies¹⁶, we therefore pursued a cascade process with CO₂-to-CO followed by CO electroreduction (COR) to *n*-propanol^{14–16} (Fig. 1b). The key challenge in advancing

¹Department of Electrical and Computer Engineering, University of Toronto, Toronto, Ontario, Canada. ²Key Laboratory of Biomass Chemical Engineering of Ministry of Education, College of Chemical and Biological Engineering, Zhejiang University, Hangzhou, China. ³Department of Mechanical and Industrial Engineering, University of Toronto, Toronto, Ontario, Canada. ⁴Beijing Synchrotron Radiation Facility, Institute of High Energy Physics, Chinese Academy of Sciences, Beijing, China. ⁵College of Chemistry and Molecular Engineering, Peking University, Beijing, China. ⁶These authors contributed equally: Yuanjun Chen, Xinyue Wang, Xiao-Yan Li, Rui Kai Miao. ✉e-mail: yhou@zju.edu.cn; sinton@mie.utoronto.ca; ted.sargent@utoronto.ca

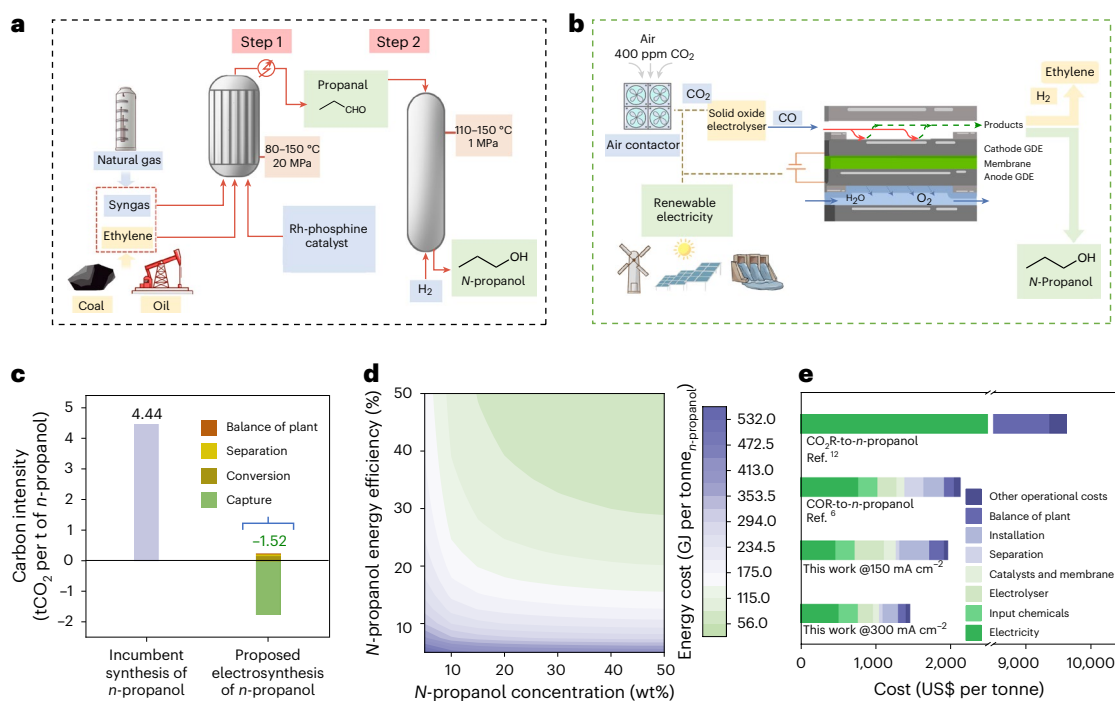


Fig. 1 | Electro-synthesis of *n*-propanol by using renewable energy. **a**, Existing thermochemical route to *n*-propanol. **b**, The proposed electrochemical system. **c**, LCA for carbon intensity of *n*-propanol production by the industrial thermochemical system and the proposed electrochemical system. Data for LCA calculation of the electrochemical system are from this work and details are shown in Supplementary Note 3. **d**, Energy consumption

for *n*-propanol production associated with *n*-propanol energy efficiency and concentration. Details are shown in Supplementary Note 1. **e**, Breakdown of the plant-gate leveled cost per tonne of *n*-propanol, as calculated from a TEA. Data for TEA calculation are from this work and refs. 6,12. Details are shown in Supplementary Note 2.

this approach is to improve COR performance towards *n*-propanol, simultaneously increasing the CO-to-*n*-propanol electrolyser energy efficiency and producing highly concentrated *n*-propanol in the final product stream¹⁷ (the latter to minimize distillation energy costs). The efficient previous reports of CO-to-*n*-propanol electro-synthesis have exhibited *n*-propanol energy efficiency of 16% with *n*-propanol concentration below 1 wt% (refs. 6,18–20). With *n*-propanol production requiring both C₁–C₁ and C₁–C₂ coupling^{21–24}, generating the relevant C₁ and C₂ intermediates on proximate active sites could offer an efficient route.

Herein we pursued a materials synthesis strategy to produce catalysts with distinct C₁- and C₂-generating active sites in close proximity. The resultant Sn–Cu dilute alloy catalyst leads to a Faradaic efficiency (FE) of 47 ± 3% and an energy efficiency of 24% in *n*-propanol production. We increased *n*-propanol concentration by reversing local electro-osmotic resistance and prolonging the diffusion pathway of *n*-propanol. By combining the catalyst strategy with electrode system engineering, we fabricated a carbon/ionomer composite layer onto the Sn–Cu catalyst to construct a catalyst/carbon/ionomer heterojunction (CCIH), and found that this suppresses *n*-propanol crossover and thus facilitates concentrated *n*-propanol collection at the cathode, leading to an *n*-propanol product concentration of 30 wt%. On the basis of our experimentally measured performance, assuming the use of wind as low-carbon electricity and assuming that CO₂ is obtained via direct air capture, we estimate cradle-to-gate –1.5 tonnes of CO₂-equivalent per tonne of *n*-propanol (tCO₂eq/t *n*-propanol) compared to today's value of +4.4 tCO₂eq/t *n*-propanol.

Results

Catalyst design for *n*-propanol electro-synthesis

We conducted an initial life cycle assessment (LCA) and studied the potential for *n*-propanol electro-synthesis systems to decarbonize *n*-propanol production when CO₂ is sourced from direct air capture

and the full system is powered using wind electricity (Fig. 1c). An accompanying technoeconomic analysis (TEA) indicates that achieving high *n*-propanol electrolyser energy efficiency and *n*-propanol concentration are critical to reduce the plant-gate leveled cost of *n*-propanol production (Fig. 1d,e, Supplementary Notes 1–3, Supplementary Figs. 1–3 and Supplementary Tables 1–3). The goal of increasing electrolyser energy efficiency motivated us to study a catalyst design that stabilizes the relevant C₁ and C₂ intermediates and facilitates C₁–C₂ coupling.

In initial studies on Cu alone, we saw the same product distribution trend as in previous reports: a mix of predominantly C₂ alongside a minor proportion of *n*-propanol with negligible presence of C₁ products (Supplementary Fig. 4). This observation suggests that on the Cu surface, C₁ intermediates primarily engage in direct coupling to form C₂ intermediates, rather than proceeding towards further hydrogenation to generate C₁ products or engaging in C₁–C₂ coupling to yield C₃ products. We therefore pursued identifying the specific C₁ intermediates conducive to C₁–C₂ coupling. When we sought to improve the *CO coverage on the Cu surface via pressurization, a slight decrease in *n*-propanol FE was observed (Supplementary Fig. 5). We propose that *CO is an intermediate to C₂, but it is not the primary C₁ intermediate of *n*-propanol. Instead, from formaldehyde-feed studies (Supplementary Figs. 6 and 7), it appears likely that intermediate(s) related to formaldehyde (for example, adsorbed formyl *CHO, adsorbed formaldehyde *CH₂O) are the key C₁ intermediates on the pathway to *n*-propanol.

This prompted us to seek a second metal with higher oxygen affinity than Cu to promote the formation and stabilization of the intermediate(s) related to formaldehyde^{25,26}. Unfortunately, when we introduced more than 10% surface coverage of high-oxygen-affinity metals (HOA-M), selectivity was lost to methane (Supplementary Tables 4–6 and Supplementary Fig. 8). This result indicates that the introduction of HOA-M leads to the generation of formaldehyde related C₁ intermediates^{26,27}. However, the presence of high-coverage HOA-M

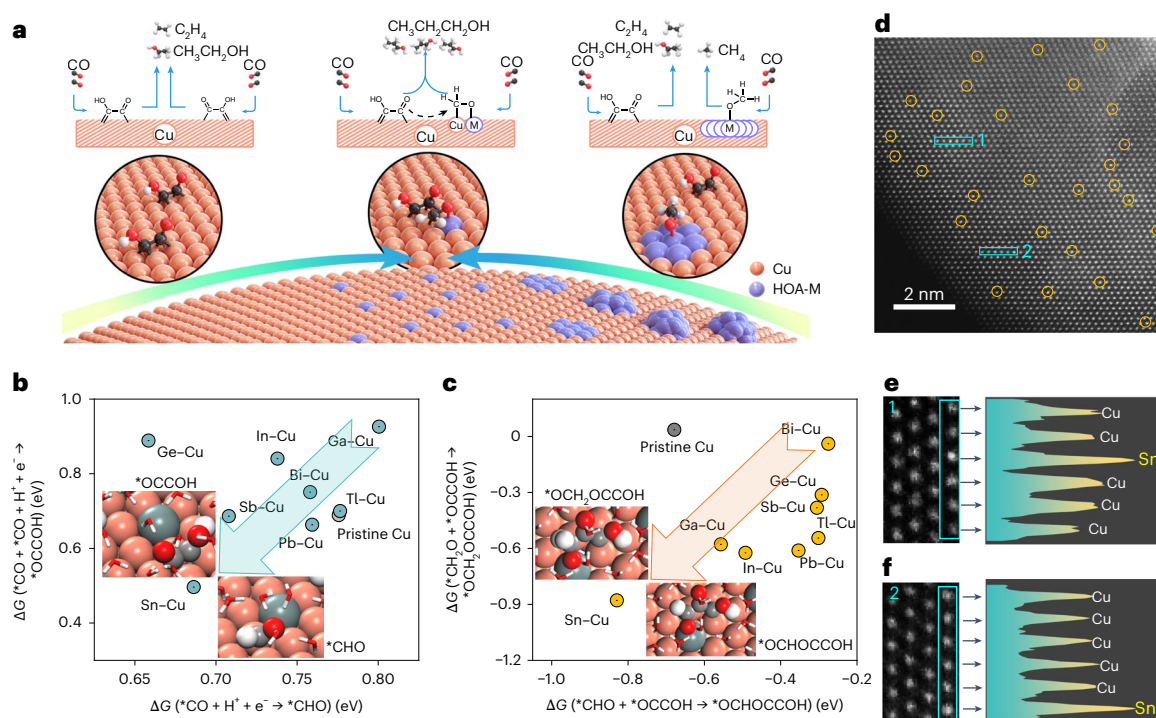


Fig. 2 | Design criteria and structure of the electrocatalyst. **a**, Catalytic strategy based on the atomic arrangement of active sites through altering the surface coverage of HOA-M on the Cu surface. The approach seeks to regulate the adsorption and activation behaviours of key C_1 and C_2 intermediates, ensuring their spatial proximity and enhancing the C_1 - C_2 coupling for improved n -propanol production. **b**, Combination of *CO hydrogenation

energy to *CHO for C_1 intermediate and $^*CO + ^*CO$ coupling energy to *OCCOH for C_2 intermediate. **c**, Combination of C_1 intermediates (*CHO and *CH_2O) + *OCCOH coupling energies for C_3 intermediates in Cu-based atomically dilute alloy catalysts. **d-f**, The aberration-corrected HAADF image of Sn-Cu atomically dilute alloy catalyst (**d**), along with intensity profiles extracted along the marked light blue rectangles 1 (**e**) and 2 (**f**).

on the Cu surface restricts the spatial availability for the coupling of C_1 intermediate with C_2 intermediate adsorbed on the Cu surface. Consequently, C_1 and C_2 intermediates undergo distinct subsequent proton-coupling electron transfer processes, leading to a mixed product distribution of C_1 (methane) and C_2 products^{27,28} (Fig. 2a).

We therefore considered the idea of altering the atomic arrangement of active sites at the atomic scale, seeking to modify the spatial adsorption configuration of surface intermediates²⁸⁻³⁰. We pursued atomically dilute HOA-M:Cu alloys with atomically adjacent distinct active sites to enable the cooperative adsorption of key C_1 and C_2 intermediates, thereby enhancing the spatial availability of C_1 - C_2 coupling (Fig. 2a).

We carried out density functional theory (DFT) calculations to screen metal-doped Cu dilute alloys, considering metal dopants with high-oxygen affinity, including p -block metals (that is, Ga, Ge, In, Sn, Sb, Tl, Pb, Bi) and Zn (Supplementary Note 4). In this way, we identified that the Sn-Cu dilute alloy with atomically dispersed Sn on the Cu surface appeared to favour *CO hydrogenation to *CH_xO ($x = 1, 2$) for C_1 intermediates, *CO dimerization to *OCCOH for C_2 intermediates, as well as C_1 - C_2 coupling, compared to other p -block metal-doped Cu dilute alloys (Fig. 2b,c and Supplementary Figs. 9-12) and the Zn-Cu dilute alloy (Supplementary Figs. 13-18 and Supplementary Note 4). DFT calculations also indicated the Sn-Cu dilute alloy drives the configuration of the C_1 intermediate from the atop-adsorption (*CH_xO -t) to favour instead the bridge-adsorption (*CH_xO -b) on adjacent Cu and Sn sites (Supplementary Fig. 19). This is expected to bring into adjacency the coupling of *CH_xO -b and *OCCOH to facilitate n -propanol production.

Materials synthesis and operando mechanistic studies

Experimentally we then synthesized Sn-Cu dilute alloys using a solvothermal-electrochemical reduction method. We also prepared

Zn-Cu, Ga-Cu, In-Cu, Sb-Cu, Pb-Cu and Bi-Cu, analogously, for comparison. Transmission electron microscopy (TEM) images of Sn-Cu exhibited a lattice spacing of 0.21 nm, corresponding to the Cu (111) facet, without crystalline Sn features (Supplementary Figs. 20 and 21). Energy dispersive spectroscopy showed a uniform dispersion of Sn and Cu (Supplementary Fig. 22). In aberration-corrected high-angle annular dark-field scanning TEM (HAADF-STEM) we were able to distinguish isolated Sn atoms highlighted by yellow circles (Fig. 2d and intensity profiles in Fig. 2e,f). We carried out in situ X-ray absorption spectroscopy (XAS) to investigate the state of the catalyst during electrochemical COR. The in situ extended X-ray absorption fine structure (EXAFS) analysis was conducted to examine the chemical structure during COR. The Cu K-edge EXAFS spectra of Sn-Cu exhibited a main peak at approximately 2.2 Å, this associated with Cu-Cu coordination (Supplementary Fig. 23), also seen via EXAFS fitting analysis (Supplementary Fig. 24 and Supplementary Table 7), indicating that Cu is in the metallic state in Sn-Cu. The Sn K-edge EXAFS spectra of Sn-Cu showed a main peak at approximately 2.2 Å ascribed to the Sn-Cu coordination, and a shoulder at approximately 1.5 Å, due to Sn-O coordination from the O species of the *CH_xO -b intermediates interacting with Sn atoms (Supplementary Fig. 25). We performed EXAFS fitting for the Sn K-edge spectra of Sn-Cu and found that these show similar trends to those predicted by the DFT model of *CH_xO -b adsorbed on Sn-Cu (Supplementary Fig. 26 and Supplementary Table 7). We did not detect Sn-Sn coordination in the Sn K-edge EXAFS spectra of Sn-Cu. These results demonstrate that Sn species are atomically dispersed on Cu matrix, forming atomically adjacent Sn-Cu dual atomic sites. Furthermore, in situ X-ray absorption near-edge fine structure (XANES) analysis was conducted to investigate the electronic structure of Sn and Cu during COR. The Cu K-edge XANES spectra of Sn-Cu showed similar white-line intensity and edge position to Cu foil (Supplementary Fig. 27), indicating that Cu species within

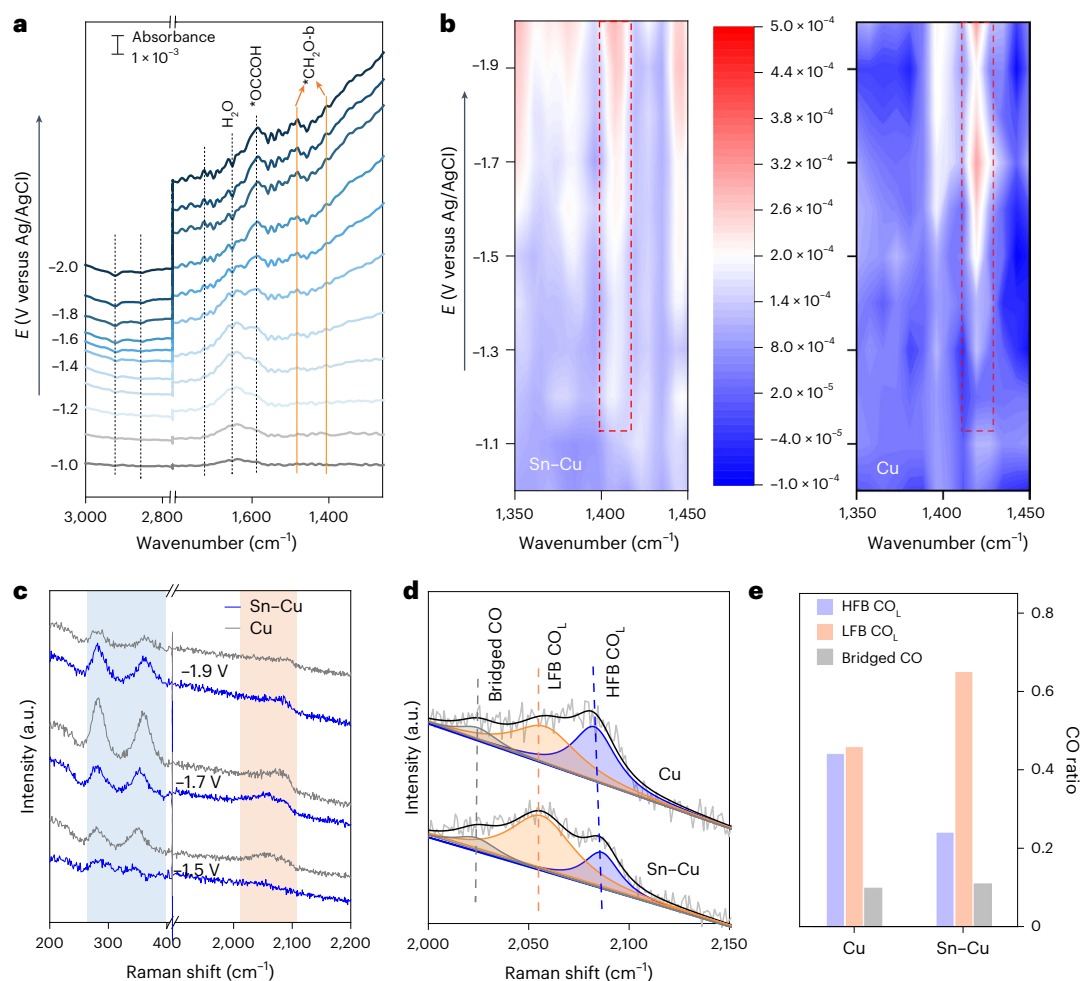


Fig. 3 | In situ ATR-SEIRAS studies. **a**, In situ ATR-SEIRS spectra recorded during COR on Sn–Cu atomically dilute alloy catalyst from -1.0 to -2.0 V versus Ag/AgCl. **b**, Contour map of in situ ATR-FTIR spectra on the Sn–Cu catalyst and Cu catalyst at the wavenumber range of $1,350$ to $1,450$ cm^{-1} . Spectra presented correspond to 64 co-added scans collected with an 8-cm^{-1} resolution. **c**, In situ Raman spectra recorded during COR on the Sn–Cu catalyst and Cu catalyst. The regions from 260 to 400 cm^{-1} associated with the surface-absorbed

CO are shaded in light blue. The regions from $2,010$ to $2,110$ cm^{-1} , corresponding to the C–O stretching of the absorbed CO are shaded in light orange. **d**, The Raman spectra analysis of the Sn–Cu catalyst and Cu catalyst in the range of $2,000$ to $2,150$ cm^{-1} . **e**, Comparison of different CO adsorption ratios on the Sn–Cu catalyst and Cu catalyst. LFB CO_L , low-frequency band linear CO; HFB CO_L , high-frequency band linear CO.

Sn–Cu exhibited metallic nature during COR. The Sn K-edge XANES spectra of Sn–Cu showed a slightly higher white-line intensity and a positive shift in edge position compared to Sn foil (Supplementary Fig. 28), suggesting the oxidation state of Sn is slightly positive, this is due to the interaction with the O species of the $^*\text{CH}_x\text{O-b}$ intermediates during COR.

We carried out in situ surface-enhanced infrared absorption spectroscopy in the attenuated total reflection mode (ATR-SEIRAS) (Fig. 3a and Supplementary Figs. 29 and 30). The peak at $1,425$ cm^{-1} in the ATR-SEIRAS spectra of the pristine Cu we assign to the C=O stretching of hydrogenated CO ($^*\text{CH}_2\text{O}$) that is stabilized through its C species interacting with the Cu surface in an upright geometry^{31,32} (Fig. 3b and Supplementary Fig. 30). In the ATR-SEIRAS spectra of the Sn–Cu atomically dilute alloy catalyst, the peak at $1,425$ cm^{-1} is red-shifted to $1,405$ cm^{-1} , indicating a longer C–O bond length on the Sn–Cu. Another peak at $1,485$ cm^{-1} is observed on the Sn–Cu, which is ascribed to the δCH_2 vibration in $^*\text{CH}_2\text{O}$ (refs. 33,34; Fig. 3a,b). This result indicates the adjacent Sn–Cu dual sites on the Sn–Cu catalyst allowed $^*\text{CH}_2\text{O}$ to be stabilized in a bridge-bound geometry ($^*\text{CH}_2\text{O-b}$) through both its O species interacting with Sn atom and its C species interacting with the Cu atom, leading to a lengthened C–O bond length. These findings from in situ ATR-SEIRAS spectra are consistent with our DFT calculation results (Supplementary Fig. 19) and XAS analysis

results (Supplementary Fig. 26 and Supplementary Table 7). In comparison, the ATR-SEIRAS spectra of the high-coverage Sn–Cu sample with 10% surface coverage of Sn exhibits distinct peaks associated with oxygen-bonded C_1 intermediates in an upright geometry (Supplementary Fig. 31). The peaks at $1,100$ and $1,128$ cm^{-1} are ascribed to the $^*\text{CHO}$ and $^*\text{OCH}_3$ groups in an upright geometry, respectively³⁵. The $^*\text{OCH}_3$ serves as a crucial intermediate in methane production²⁷. These observations align with performance, where the production of methane was seen in the high-coverage Sn–Cu sample (Supplementary Fig. 32).

The CO stretching bands at $1,562$ and $1,713$ cm^{-1} ascribed to $^*\text{OCCOH}$ are observed in the Sn–Cu (ref. 36); these increased with the applied potential (Fig. 3a). We offer that in the Sn–Cu atomically dilute alloy catalyst system, bridge-bound $^*\text{CH}_2\text{O-b}$ adsorbed on adjacent Sn–Cu dual sites is attacked by $^*\text{OCCOH}$ adsorbed on neighbouring Cu sites to produce n -propanol through C_1 – C_2 coupling and subsequent proton-coupling electron transfer processes.

In situ Raman spectra bands located at roughly 283 and 363 cm^{-1} are associated with the frustrated rotation of $^*\text{CO}$ on Cu and the Cu–CO stretching, respectively^{37,38}. We observed no shifts in the Cu–CO stretching band on Sn–Cu under applied potentials (Fig. 3c). This suggests that Sn doping has only a minor effect on Cu–CO adsorption³⁹, which, coupled with increased n -propanol production on Sn–Cu,

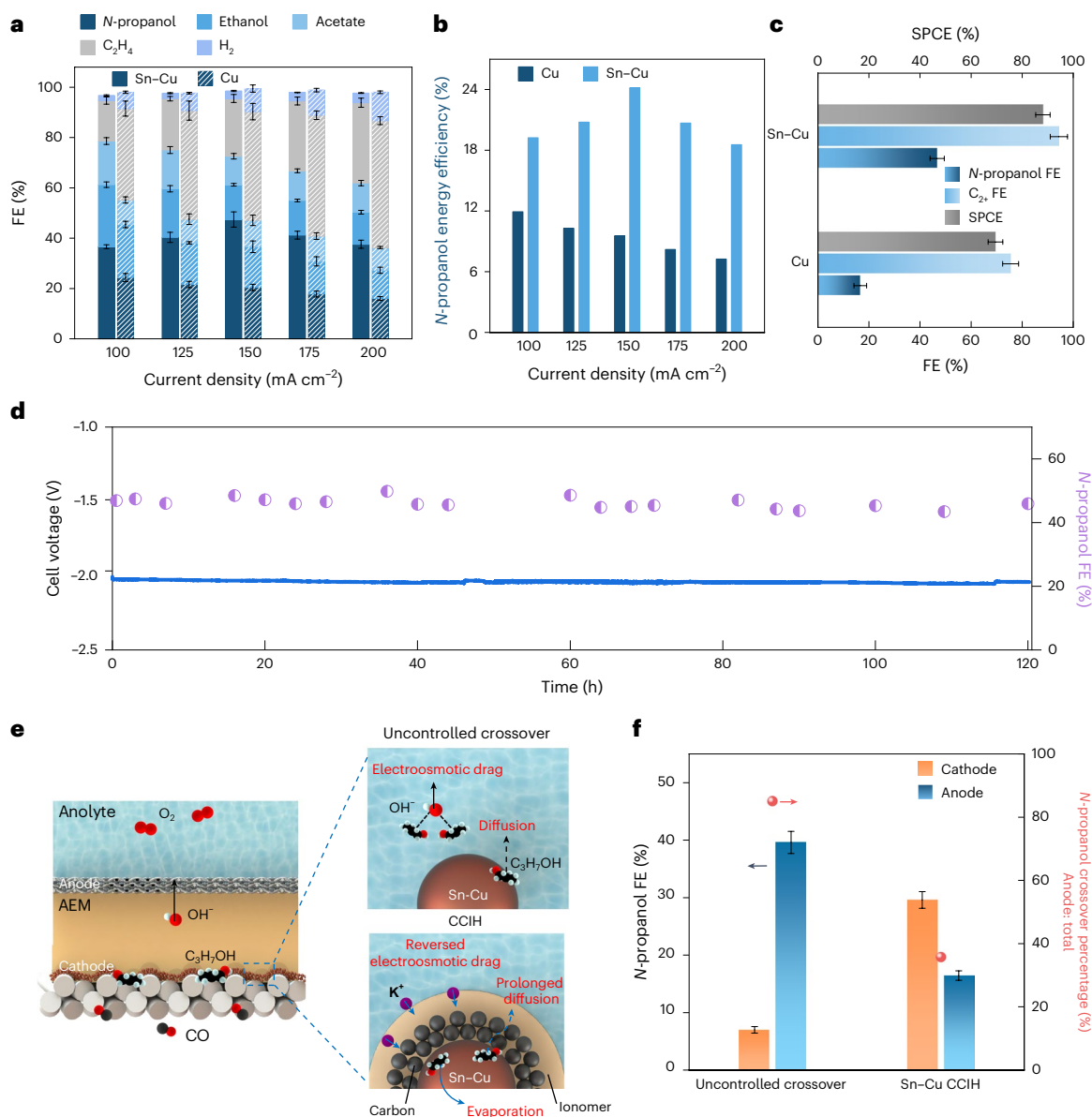


Fig. 4 | Performance of *n*-propanol production on the Sn–Cu atomically dilute alloy catalyst. a, Product distribution in COR on the Sn–Cu and the pristine Cu under different current densities. The FE values are means and error bars represent the standard deviation from three independent measurements ($n = 3$). **b**, *N*-propanol energy efficiency and full-cell voltage of Sn–Cu and the pristine Cu in MEA electrolyser. **c**, *N*-propanol FE, C_{2x} FE and SPCE of the Sn–Cu and the pristine Cu catalyst under 16 sccm CO flow rate at the current of 2.4 A in an area of 16 cm² MEA electrolyser. The values are means and error bars represent the standard deviation from three independent measurements ($n = 3$). **d**, One hundred twenty hours of stability at a total current density of 150 mA cm⁻² on

the Sn–Cu catalyst. The purple half-filled circle represents the *n*-propanol FE and the blue solid line represents the cell voltage of the Sn–Cu catalyst at a total current density of 150 mA cm⁻². **e**, Schematic illustration of CCIH architecture for suppressing crossover and facilitating concentrated *n*-propanol. AEM, anion-exchange membrane. **f**, *N*-propanol FE at cathode and anode sides comparing the uncontrolled crossover and the Sn–Cu CCIH architecture operating at 40 °C. Experimental data obtained using a Sn–Cu electrode (uncontrolled crossover) and a Sn–Cu CCIH electrode at 150 mA cm⁻² in 3 M KOH. The FE values are means and error bars represent the standard deviation from three independent measurements ($n = 3$).

suggests that adsorbed *CO is not the primary C₁ intermediate for *n*-propanol. A set of bands at 2,000–2,150 cm⁻¹ in the C–O stretching region can be further deconvoluted into three peaks associated with different adsorption configurations: bridged CO, the low-frequency band (LFB) and the high-frequency band (HFB) linear CO, which are centred at approximately 2,030, 2,060 and 2,090 cm⁻¹, respectively. Raman spectra of Sn–Cu versus pristine Cu at –1.7 V, the potential showing the highest *n*-propanol production (Fig. 3d), showed a dominance of LFB CO on Sn–Cu, 1.5× higher than on Cu (Fig. 3e). LFB CO is typically associated with adsorbed CO species that favour C–C coupling^{40–42}.

Electrocatalytic *n*-propanol electrosynthesis

We evaluated electrochemical COR performance in a membrane-electrode assembly (MEA) electrolyser. We optimized the catalyst loading and the concentration of electrolyte (Supplementary Figs. 33–35). Using the optimized Sn–Cu atomically dilute alloy electrode in 3 M KOH, we achieved a C_{2x} FE of over 96% and H₂ FE of 4% and below across a current density range 100–200 mA cm⁻² (Fig. 4a and Supplementary Tables 8 and 9). The Sn–Cu electrode showed a peak *n*-propanol FE of 47 ± 3% at 150 mA cm⁻², leading to a 24% *n*-propanol energy efficiency (Fig. 4b and Supplementary Fig. 36). This energy efficiency achieved on the Sn–Cu electrode is 1.5 times higher than that reported in the most

efficient previous *n*-propanol electrosynthesis studies (Supplementary Figs. 37 and 38 and Supplementary Table 10). Pristine Cu exhibited a maximum 24% FE and 12% energy efficiency towards *n*-propanol at 100 mA cm⁻². For comparison, we also assessed the performance of Zn–Cu, Ga–Cu, In–Cu, Sb–Cu, Pb–Cu and Bi–Cu (Supplementary Fig. 39), and the *n*-propanol FE remains highest on Sn–Cu, in agreement with DFT calculations.

We sought to increase the CO single-pass conversion efficiency (SPCE) by optimizing electrode geometry, and we reached 88% SPCE to C₂₊ products, simultaneous with 47 ± 3% *n*-propanol FE in a 16 cm² electrocatalysis system (Fig. 4c). To evaluate initial stability, we studied 120-h operation in the MEA electrolyser (Fig. 4d); both voltage and FE changed no more than 7% (relative) over this duration of operation. We then conducted postreaction X-ray diffraction (XRD) and X-ray photoelectron spectroscopy (XPS) measurements to investigate the oxidation state of Sn and Cu. Three main peaks corresponding to the crystal planes of (111), (200) and (220) of metallic Cu were observed in the XRD patterns of the postreaction Sn–Cu (Supplementary Fig. 40). The Cu 2*p* XPS spectra of the postreaction Sn–Cu exhibited two main peaks at binding energies of 932 and 951.8 eV, attributed to the 2*p*_{3/2} and 2*p*_{1/2} states of metallic Cu (Supplementary Fig. 41). Similarly, in the Sn 3*d* XPS spectra of Sn–Cu, two main peaks were observed at binding energies of 485.1 and 493.5 eV, corresponding to the 3*d*_{5/2} and 3*d*_{3/2} states of metallic Sn (Supplementary Fig. 42). These results indicate the metallic nature of Cu and Sn species within Sn–Cu was well-maintained.

Construction of a Sn–Cu CCIH to achieve high *n*-propanol concentration

Previous reports of *n*-propanol electrosynthesis concentration have been below 1 wt%, the result of uncontrolled *n*-propanol crossover through anion-exchange membranes via electro-osmotic drag and diffusion^{43,44}. Studying the crossover of *n*-propanol, we found that across current densities most (more than 85%) of the *n*-propanol crosses the anion-exchange membrane into the anode and is markedly diluted in the anolyte (Supplementary Figs. 43 and 44). Concentrating the product is of interest to minimize downstream separation energy^{17,45}. We first studied a Sn–Cu catalyst/ionomer heterojunction (CIH) and found a reduction in *n*-propanol crossover from 85 to 66% (Supplementary Fig. 45). Cross-sectional scanning electron microscopy analysis revealed that the ionomer forms a thin (<1 μm) adlayer on top the Sn–Cu catalyst (Supplementary Fig. 46). We proposed that the anionic charged adlayer reverses the ionic flux locally, forming a locally high concentration of cations near the catalyst and reducing electro-osmotic drag of *n*-propanol to the anode (Fig. 4e).

To reduce crossover further, we aimed to further address the diffusion of the *n*-propanol into the anode. We further constructed a Sn–Cu CCIH architecture (Fig. 4e). The *n*-propanol production remained similar with the addition of the carbon/ionomer adlayer (Supplementary Fig. 47). Scanning electron microscopy images of the Sn–Cu CCIH revealed that the carbon/ionomer adlayer forms a highly porous structure approximately 10 μm thick (Supplementary Fig. 46c). The porous structure increases tortuosity, further prolonging the pathways for *n*-propanol diffusion. Together with the ionomer, the CCIH reduced *n*-propanol crossover from 85 to 35% and achieved 30 wt% *n*-propanol on the cathode (Fig. 4e,f and Supplementary Figs. 48–50). Studying the effect of electrolyte concentrations, we found that *n*-propanol crossover is mostly unaffected by the electrolyte concentration (Supplementary Fig. 51). The system operated stably (change in FE and full-cell voltages were less than 10% relative) and produced *n*-propanol over 30 wt% in the course of 120 h (Supplementary Fig. 52). Structural characterization after the 120 h of operation showed that the structure of the Sn–Cu catalyst was well preserved (Supplementary Figs. 53–55 and Supplementary Note 5).

Conclusions

This work reports a dilute alloy catalyst that stabilizes relevant C₁ and C₂ intermediates via proximate active sites. By combining this catalyst design strategy with electrode system engineering, a Sn–Cu dilute alloy catalyst implemented in a CCIH architecture, we document *n*-propanol FE of 47 ± 3%, product concentration of 30 wt%, single-pass CO conversion of 88% and electrolyser energy efficiency of 24% at 150 mA cm⁻², united with 120 h of stability in a MEA electrolyser. LCA and TEA indicate the potential of *n*-propanol produced in this manner to contribute to the decarbonization of chemical production.

Methods

Chemicals

Copper(II) sulfate pentahydrate (CuSO₄·5H₂O), tin(IV) chloride pentahydrate (SnCl₄·5H₂O), sodium hydroxide (NaOH), potassium hydroxide (KOH), methanol, formaldehyde and Nafion perfluorinated resin solution (5 wt% in a mixture of lower aliphatic alcohols and water) were purchased from Sigma Aldrich. Carbon black, acetylene, 100% compressed was obtained from Thermo Scientific Chemicals. Sustainion anion-exchange membrane was obtained from Dioxide Materials. Titanium mesh was obtained from the Fuel Cell Store. The polytetrafluoroethylene (PTFE) gas-diffusion layer with 450-nm pore size was purchased from Beijing Zhongxingweiye Instrument Co., Ltd. The copper target (>99.99%) was obtained from K. J. Lesker. The aqueous solutions in all the experiments were prepared using distilled water with a resistivity of 18.2 MΩ·cm obtained from a Milli-Q reference water-purification system.

Material synthesis

The typical synthesis of Sn–Cu atomically dilute alloy catalyst is taken as an example. Four millimoles of CuSO₄·5H₂O and 0.025 mmol of SnCl₄·5H₂O were dissolved in 50 ml of distilled water in a flask and then immersed in an ice water bath with vigorous stirring. Then, 10 ml of 1.2 M NaOH solution was added dropwise, and the mixture was vigorously stirred for 30 min. Followed by being refrigerated at about 3 °C for 24 h, the mixture was transferred into a 100 ml of Teflon-lined autoclave and heated at 130 °C for 20 h. The resulting precipitate was obtained by washing repeatedly with distilled water, and then dried in a vacuum at 60 °C for 12 h. The resulting powder was calcined at 400 °C for 3 h to obtain the preformed Sn–CuO. The Sn–Cu atomically dilute alloy catalyst was prepared by an electrochemical reduction of the preformed Sn–CuO running for 30 min under in situ COR at 50 mA cm⁻². The Sn–Cu catalysts with different Sn surface coverages on Cu were obtained using a similar procedure, except that the feeding molar ratios of the Sn or Cu metal precursors were increased to 1:13, 2:11 and 1:3, respectively, while maintaining a consistent total feed of 4 mmol. The Cu catalyst was obtained using a similar procedure without the inclusion of a Sn precursor. The Zn–Cu, Sb–Cu, In–Cu, Bi–Cu, Pb–Cu and Ga–Cu catalysts were obtained using a similar procedure to the Sn–Cu atomically dilute alloy catalyst, except that the SnCl₄·5H₂O was replaced with Zn(NO₃)₂·6H₂O, SbCl₃, InCl₃, BiCl₃, Pb(NO₃)₂ and Ga(NO₃)₃, respectively.

Electrode preparation

The homemade conductive gas-diffusion layer was prepared by sputtering a 200-nm-thick copper layer onto a PTFE substrate at a sputtering rate of 1 Å s⁻¹ using a pure copper target in an Angstrom Nexdep sputtering system. For the preparation of the Sn–Cu electrode, the catalyst ink consisting of 40 mg of as-prepared Sn–CuO powder, 120 μl of 5 wt% Nafion perfluorinated resin solution and 4 ml of methanol was ultrasonicated for 2 h and then was spray-coated onto a homemade conductive gas-diffusion layer with Sn–CuO loading of 1.6 mg cm⁻². The loading was determined by weighing the electrode before and after spraying. The Sn–Cu electrode was finally obtained by an electrochemical reduction of the preformed Sn–CuO running for 30 min under in situ

COR at 50 mA cm⁻². The preparation of the Cu electrode was followed by a similar procedure except that as-prepared CuO powder was used and the catalyst loading was ensured to be consistent. To fabricate the Sn–Cu CCIH, an ink consisting of 40 mg of carbon particles (carbon black, acetylene, 100% compressed, Thermo Scientific Chemicals), 350 mg of ionomer (5 wt% Nafion perfluorinated resin solution) and 4 ml of methanol was spray-coated as a carbon/ionomer adlayer onto the Sn–Cu electrode. The ink was ultrasonicated for 2 h before spray coating. The loading of the carbon/ionomer adlayer was determined by weighing the electrode before and after spraying.

Materials characterization

The morphologies of samples were characterized by TEM (Hitachi HF3300) (JEOL-2100F). The high-resolution TEM images and the corresponding elemental energy dispersive spectroscopy mappings were obtained using a JEOL JEM-2100F with an electron acceleration energy of 200 kV. The aberration-corrected HAADF-STEM images were obtained on a high-resolution TEM (JEOL JEM-ARM200F working at 300 kV), equipped with a probe spherical aberration corrector. The inductively coupled plasma optical emission spectroscopy (iCAP6300) was used to measure the metal content of the catalysts. Powder XRD data were obtained in transmission geometry on a STOE-STADIP powder diffractometer operating at 40-kV voltage and 40-mA current with Cu-K α 1 X-ray radiation ($\lambda = 0.154056$ nm). XPS measurements were used to determine the Sn coverage on Cu surface in the Sn–Cu catalysts with different Sn content by using an ECSA device (PHI5700) with an Al K α energy source (1,486.6 eV) for excitation. The metal content of the catalysts was measured by ICP-OES (iCAP6300). XAS data were collected at the 9BM beamline of the Advanced Photon Source (Argonne National Laboratory, Lemont, IL, USA). In situ XAS measurements were conducted using a homemade flow cell⁴⁶. The Ag/AgCl electrode served as the reference electrode and a Ni foam served as the counter electrode. The Sn–Cu electrode or Cu electrode was used as a working electrode. During testing, CO was flowed through the gas compartment with a constant flow rate of 20 sccm, while 3 M KOH solution was circulated through the cathode and anode compartments at flow rates of 10 ml min⁻¹, respectively. The in situ XAS data were collected under a constant current density of 150 mA cm⁻². The XAS raw data were background-subtracted and Fourier-transformed by the standard procedures with the ATHENA software. The least-squares curve-fitting analysis of the EXAFS $\chi(k)$ data was carried out using the ARTEMIS programme based on the standard EXAFS equation. All fits were conducted in the R space with a k weight of 2, and the fitting parameter values are listed in Supplementary Table 7. In situ Raman measurements were performed in a Renishaw inVia Raman microscope equipped with a water immersion objective ($\times 63$) and a 785-nm laser in a modified flow cell. A BRUKER INVENIO R spectrometer equipped with a liquid nitrogen-cooled mercury cadmium telluride detector was used for the in situ ATR-SEIRAS measurements. Spectral resolution was set at 8.0 cm⁻¹ and each spectrum incorporated 64 interferograms.

Electrochemical measurements

Electrochemical measurements were evaluated in the MEA electrolyser (SKU 68732; Dioxide Materials) consisting of a gas chamber and an anodic chamber. Titanium mesh-supported iridium oxide (IrO_x/Ti mesh) was used as the anode electrode and was prepared by a previously reported dip coating and thermal decomposition method⁴⁷. Since the PTFE side of the homemade conductive gas-diffusion layer is non-conductive, the cathode electrode was fixed onto the gas chamber using copper tape to ensure good electrical conduction with the titanium plate of the MEA electrolyser. Subsequently, the activated anion-exchange membrane (Sustainion X37-50 Grade RT, Dioxide Materials), silicone gasket and IrO_x/Ti mesh anode catalyst were placed on the top of the cathode. Finally, the electrolyser was assembled with a torque wrench. We used an electrochemical station (Autolab

PGSTAT302N) equipped with a current booster (Metrohm Autolab, 10 A) for performance measurements. Then 3 M KOH was used as the anolyte that was circulated through the anode chamber using peristaltic pumps at a rate of 10 ml min⁻¹. CO gas with different feed flowing rate controlled by a digital gas flow controller flowed to the humidifier with distilled water, then supplied to the gas chamber. Unless explicitly stated otherwise, all the COR measurements were conducted in a 1-cm² MEA electrolyser in 3 M KOH with a CO flow rate of 20 sccm. To pursue to increase the CO SPCE, we optimized electrode geometry using a 16-cm² MEA electrolyser and used a CO flow rate of 10.8 sccm. In all the electrochemical measurements, a gas chromatograph (PerkinElmer Clarus 600) with a flame ionization detector and a thermal conductivity detector was used to analyse the gas products, collected from the end of the gas chamber. 1H nuclear magnetic resonance spectroscopy (600 MHz Agilent DD2 NMR Spectrometer) with water suppression was used to analyse the liquid products, using dimethyl sulfoxide as the reference standard and deuterium oxide (D₂O) as the lock solvent. Liquid products were collected from anode and cathode sides during the electrolysis.

The CO single-pass carbon efficiency (SPCE) under the conditions of 298.15 K and 101.3 kPa was determined using the following equation:

$$\text{SPCE} = [(j \times 60 \text{ s}) / (N \times F)] / \left[\left(\text{flow rate} \left(\frac{1}{\text{min}} \right) \times 1(\text{min}) \right) / \left(24.05 \left(\frac{1}{\text{min}} \right) \right) \right] \quad (1)$$

where j is the partial current density of a specific product from COR and N is the electron transfer for every product molecule.

The full-cell energy efficiency (EE) based on the production of n -propanol was calculated as follows:

$$\text{EE}_{\text{full cell}, n\text{-propanol}} = \frac{(1.23 + (-E_{n\text{-propanol}}^0)) \times \text{FE}_{n\text{-propanol}}}{-E_{\text{full cell}}} \quad (2)$$

where $E_{n\text{-propanol}}^0$ ($E_{n\text{-propanol}}^0 = 0.20$ V versus RHE) is the thermodynamic potential of CO to n -propanol, $\text{FE}_{n\text{-propanol}}$ is the measured FE of n -propanol and $E_{\text{full cell}}$ is the full-cell voltage without ohmic loss correction evaluated in the MEA electrolyser.

Computational methods

The Vienna Ab initio Simulation Package was used to perform all spin unrestricted DFT calculations^{48,49}. The Perdew–Burke–Ernzerhof formulation of the generalized gradient approximation was adopted to determine the exchange–correlation energy⁵⁰. We constructed the plane wave using a projector augmented wave⁵¹. The cut-off energy was set to 450 eV (ref. 52). The DFT-D3 method from Grimme was derived from the long-range dispersion correction⁵³. Here, a four-layer (3×3) Cu(111) model with a water layer was constructed, and the bottom two layers were fixed to mimic the bulk and the other atoms are relaxed²⁴. To construct the Cu-based dilute alloys, we performed substitution doping for DFT modelling. Specifically, for the screened p -block metal-doped Cu-based dilute alloys and the Zn-doped Cu dilute alloy, one Cu atom on the top layer was substituted with Ga, Ge, Cu, In, Sn, Sb, Tl, Pb, Bi and Zn, respectively, based on our previous studies²⁴. Each periodic slab was separated by the vacuum space with about 15 Å along the z axis. The $3 \times 3 \times 1$ k -point mesh was generated by Monkhorst–Pack scheme in the Brillouin scheme⁵⁴. Considering the solvation and field effects in electrocatalysis, we constructed one charged water layer consisting of five water molecules and one hydronium molecule in the periodic Cu(3×3) cell⁵⁵. For the structural optimization, the self-consistent energy and force converge to below 10^{-5} eV and 0.05 eV Å⁻¹, respectively. Here, we consider four possible elementary steps to screen the candidate for C₃ products, as follows.





Here, Gibbs free energy (G) was calculated and corrected by the following equation:

$$G = E_{\text{DFT}} + \text{ZPE} + \int C_p dT - TS \quad (7)$$

where E_{DFT} , ZPE, $\int C_p dT$ and TS are the contribution from electronic energy directly calculated by DFT, zero-point energy, temperature enthalpic and entropic correction ($T = 300 \text{ K}$), respectively. Using the computational hydrogen electrode model, the Gibbs free energy for a proton and an electron ($G(\text{H}^+ + \text{e}^-)$) in the electrolyte was treated by the half of the Gibbs free energy of molecule H_2 ($0.5 G(\text{H}_2)$) (ref. 56).

Data availability

Data supporting the findings of this study are available from the corresponding authors upon reasonable request. Source data are provided with this paper.

References

- Leow, W. R. et al. Chloride-mediated selective electrosynthesis of ethylene and propylene oxides at high current density. *Science* **368**, 1228–1233 (2020).
- Use of Energy Explained: Energy Use in Industry (US Energy Information Administration (EIA), 2019); www.eia.gov/energyexplained/use-of-energy/industry.php
- Achakulwisut, P. et al. Global fossil fuel reduction pathways under different climate mitigation strategies and ambitions. *Nat. Commun.* **14**, 5425 (2023).
- Propanol Market Size, Share & Trends Analysis Report by Product by Application (N-propanol, Isopropyl Alcohol), by Region, and Segment Forecasts, 2023–2030 (Grand View Research, 2023); <https://www.grandviewresearch.com/industry-analysis/propanol-market>
- Lepore, A. W. et al. Catalytic dehydration of biomass derived 1-propanol to propene over M-ZSM-5 (M=H, V, Cu, or Zn). *Ind. Eng. Chem. Res.* **56**, 4302–4308 (2017).
- Wang, X. et al. Efficient electrosynthesis of *n*-propanol from carbon monoxide using a Ag-Ru-Cu catalyst. *Nat. Energy* **7**, 170–176 (2022).
- Klabunde, J., Bischoff, C. & Papa, A. J. *Ullmann's Encyclopedia of Industrial Chemistry* (Wiley, 2018).
- Motte, J. et al. Environmental performance assessment of a novel process concept for propanol production from widely available and wasted methane sources. *Ind. Eng. Chem. Res.* **61**, 11071–11079 (2022).
- Gehrmann, S. & Tenhumberg, N. Production and use of sustainable C₂-C₄ alcohol – an industrial perspective. *Chem. Ing. Tech.* **92**, 1444–1458 (2020).
- Nabil, S. K., McCoy, S. & Kibria, M. G. Comparative life cycle assessment of electrochemical upgrading of CO₂ to fuels and feedstocks. *Green Chem.* **23**, 867–880 (2021).
- Shin, H., Hansen, K. U. & Jiao, F. Techno-economic assessment of low-temperature carbon dioxide electrolysis. *Nat. Sustain.* **4**, 911–919 (2021).
- Jeong, S. et al. Facet-defined dilute metal alloy nanorods for efficient electroreduction of CO₂ to *n*-propanol. *J. Am. Chem. Soc.* **146**, 4508–4520 (2024).
- Jouny, M., Luc, W. & Jiao, F. General techno-economic analysis of CO₂ electrolysis systems. *Ind. Eng. Chem. Res.* **57**, 2165–2177 (2018).
- Ozden, A. et al. Cascade CO₂ electroreduction enables efficient carbonate-free production of ethylene. *Joule* **5**, 706–719 (2021).
- Jouny, M., Hutchings, G. S. & Jiao, F. Carbon monoxide electroreduction as an emerging platform for carbon utilization. *Nat. Catal.* **2**, 1062–1070 (2019).
- Jin, J. et al. Constrained C₂ adsorbate orientation enables CO-to-acetate electroreduction. *Nature* **617**, 724–729 (2023).
- Zhu, P. & Wang, H. High-purity and high-concentration liquid fuels through CO₂ electroreduction. *Nat. Catal.* **4**, 943–951 (2021).
- Pang, Y. et al. Efficient electrocatalytic conversion of carbon monoxide to propanol using fragmented copper. *Nat. Catal.* **2**, 251–258 (2019).
- Niu, W. et al. Pb-rich Cu grain boundary sites for selective CO-to-*n*-propanol electroconversion. *Nat. Commun.* **14**, 4882 (2023).
- Pelayo Garcíade Arquer, F. et al. CO₂ electrolysis to multicarbon products at activities greater than 1A cm⁻². *Science* **367**, 661–666 (2020).
- Wang, X. et al. Efficient upgrading of CO to C₃ fuel using asymmetric C-C coupling active sites. *Nat. Commun.* **10**, 5186 (2019).
- Nitopi, S. et al. Progress and perspectives of electrochemical CO₂ reduction on copper in aqueous electrolyte. *Chem. Rev.* **119**, 7610–7672 (2019).
- Hori, Y., Takahashi, R., Yoshinami, Y. & Murata, A. Electrochemical reduction of CO at a copper electrode. *J. Phys. Chem. B* **101**, 7075–7081 (1997).
- Pablo-García, S. et al. Mechanistic routes toward C₃ products in copper-catalysed CO₂ electroreduction. *Catal. Sci. Technol.* **12**, 409–417 (2022).
- Vasileff, A., Xu, C., Jiao, Y., Zheng, Y. & Qiao, S.-Z. Surface and interface engineering in copper-based bimetallic materials for selective CO₂ electroreduction. *Chem* **4**, 1809–1831 (2018).
- Kepp, K. P. A quantitative scale of oxophilicity and thiophilicity. *Inorg. Chem.* **55**, 9461–9470 (2016).
- Peterson, A. A., Abild-Pedersen, F., Studt, F., Rossmeisl, J. & Nørskov, J. K. How copper catalyzes the electroreduction of carbon dioxide into hydrocarbon fuels. *Energy Environ. Sci.* **3**, 1311–1315 (2010).
- Hansen, H., Shi, C., Lausche, A., Peterson, A. & Nørskov, J. K. Bifunctional alloys for the electroreduction of CO₂ and CO. *Phys. Chem. Chem. Phys.* **18**, 9194–9201 (2016).
- Guo, Y., Wang, M., Zhu, Q., Xiao, D. & Ma, D. Ensemble effect for single-atom, small cluster and nanoparticle catalysts. *Nat. Catal.* **5**, 766–776 (2022).
- Hai, X. et al. Geminal-atom catalysis for cross-coupling. *Nature* **622**, 754–760 (2023).
- Millar, G. J., Rochester, C. H. & Waugh, K. C. An FTIR study of the adsorption of formic acid and formaldehyde on potassium-promoted Cu/SiO₂ catalysts. *J. Catal.* **155**, 52–58 (1995).
- Katayama, Y. et al. An in situ surface-enhanced infrared absorption spectroscopy study of electrochemical CO₂ reduction: selectivity dependence on surface C-bound and O-bound reaction intermediates. *J. Phys. Chem. C* **123**, 5951–5963 (2018).
- Popova, G. Y., Andrushkevich, T., Chesalov, Y. A. & Stoyanov, E. In situ FTIR study of the adsorption of formaldehyde, formic acid, and methyl formate at the surface of TiO₂ (anatase). *Kinet. Catal.* **41**, 805–811 (2000).
- Liu, Y.-Y. et al. Insight into the effect of the *d*-orbital energy of copper ions in metal-organic frameworks on the selectivity of electroreduction of CO₂ to CH₄. *ACS Catal.* **12**, 2749–2755 (2022).

35. Li, X. et al. Selective visible-light-driven photocatalytic CO₂ reduction to CH₄ mediated by atomically thin CuIn₅S₈ layers. *Nat. Energy* **4**, 690–699 (2019).
36. Yao, K. et al. Mechanistic insights into OC–COH coupling in CO₂ electroreduction on fragmented copper. *J. Am. Chem. Soc.* **144**, 14005–14011 (2022).
37. Li, F. et al. Cooperative CO₂-to-ethanol conversion via enriched intermediates at molecule-metal catalyst interfaces. *Nat. Catal.* **3**, 75–82 (2020).
38. Gunathunge, C. M., Ovalle, V. J., Li, Y., Janik, M. J. & Waegle, M. M. Existence of an electrochemically inert CO population on Cu electrodes in alkaline pH. *ACS Catal.* **8**, 7507–7516 (2018).
39. Fielicke, A., Gruene, P., Meijer, G. & Rayner, D. M. The adsorption of CO on transition metal clusters: a case study of cluster surface chemistry. *Surf. Sci.* **603**, 1427–1433 (2009).
40. An, H. et al. Sub-second time-resolved surface-enhanced Raman spectroscopy reveals dynamic CO intermediates during electrochemical CO₂ reduction on copper. *Angew. Chem. Int. Ed.* **60**, 16576–16584 (2021).
41. Li, H., Wei, P., Gao, D. & Wang, G. In situ Raman spectroscopy studies for electrochemical CO₂ reduction over Cu catalysts. *Curr. Opin. Green Sustain. Chem.* **36**, 100589 (2022).
42. Wei, P. et al. Coverage-driven selectivity switch from ethylene to acetate in high-rate CO₂/CO electrolysis. *Nat. Nanotechnol.* **18**, 299–306 (2023).
43. Wang, N. et al. Suppressing the liquid product crossover in electrochemical CO₂ reduction. *SmartMat* **2**, 12–16 (2021).
44. Miao, R. K. et al. Electroosmotic flow steers neutral products and enables concentrated ethanol electroproduction from CO₂. *Joule* **5**, 2742–2753 (2021).
45. Robb, A. et al. Concentrated ethanol electrosynthesis from CO₂ via a porous hydrophobic adlayer. *ACS Appl. Mater. Inter.* **14**, 4155–4162 (2022).
46. Li, J. et al. Copper adparticle enabled selective electrosynthesis of *n*-propanol. *Nat. Commun.* **9**, 4614 (2018).
47. Luc, W., Rosen, J. & Jiao, F. An Ir-based anode for a practical CO₂ electrolyzer. *Catal. Today* **288**, 79–84 (2017).
48. Kresse, G. & Hafner, J. Ab initio molecular dynamics for liquid metals. *Phys. Rev. B* **47**, 558 (1993).
49. Kresse, G. & Furthmüller, J. Efficient iterative schemes for ab initio total-energy calculations using a plane-wave basis set. *Phys. Rev. B* **54**, 11169 (1996).
50. Perdew, J. P., Burke, K. & Ernzerhof, M. Generalized gradient approximation made simple. *Phys. Rev. Lett.* **77**, 3865 (1996).
51. Kresse, G. & Joubert, D. From ultrasoft pseudopotentials to the projector augmented-wave method. *Phys. Rev. B* **59**, 1758 (1999).
52. Blöchl, P. E., Jepsen, O. & Andersen, O. K. Improved tetrahedron method for Brillouin-zone integrations. *Phys. Rev. B* **49**, 16223 (1994).
53. Grimme, S. Semiempirical GGA-type density functional constructed with a long-range dispersion correction. *J. Comput. Chem.* **27**, 1787–1799 (2006).
54. Monkhorst, H. J. & Pack, J. D. Special points for Brillouin-zone integrations. *Phys. Rev. B* **13**, 5188 (1976).
55. Montoya, J. H., Shi, C., Chan, K. & Nørskov, J. K. Theoretical insights into a CO dimerization mechanism in CO₂ electroreduction. *J. Phys. Chem. Lett.* **6**, 2032–2037 (2015).
56. Nørskov, J. K. et al. Origin of the overpotential for oxygen reduction at a fuel-cell cathode. *J. Phys. Chem. B* **108**, 17886–17892 (2004).

Acknowledgements

We acknowledge funding support from the Natural Sciences and Engineering Research Council (NSERC) of Canada. This research used

synchrotron resources of the Advanced Photon Source, an Office of Science User Facility operated for the US Department of Energy, Office of Science by Argonne National Laboratory, and was supported by the US Department of Energy under contract no. DE-AC02-06CH11357 as well as by the Canadian Light Source and its funding partners. DFT calculations were performed on the Niagara supercomputer at the SciNet HPC Consortium. SciNet is funded by: the Canada Foundation for Innovation; the Government of Ontario; the Ontario Research Fund—Research Excellence and the University of Toronto. X.W. acknowledges the Zhejiang University Excellent Doctoral Dissertation Funding. W.N. acknowledges financial support from the Swiss National Science Foundation (SNSF) Postdoctoral Mobility Fellowship (grant no. P500PN_202906).

Author contributions

E.H.S. and D.S. supervised the project. Y.C. conceived the idea, designed and conducted the experiments, and wrote the paper. X.W. carried out the experiments and contributed to data analysis and paper writing. X.-Y.L. performed the DFT calculations. R.K.M. performed experiments for the CCIH catalyst system, TEA and LCA. J.D. contributed to XAS data analysis. Z.Z. and C.L. contributed to in situ ATR-SEIRAS measurements. S.C. contributed to material characterizations. J.E.H. contributed to in situ Raman measurements. J.W. contributed to TEA. W.N. contributed to XAS measurements. P.O. assisted with DFT calculations. Z.G. and Y.X. contributed to CCIH catalyst system. B.X. and Y.H. contributed to data analysis and discussions and paper preparation. All authors discussed the results and assisted with paper preparation.

Competing interests

There is a US provisional patent application (63/584,253) titled ‘Processes and systems for the electrochemical reduction of carbon monoxide to propanol, cathode catalysts and cathodes used in the same’ filed by the authors Y.C., X.W., R.K.M., D.S. and E.H.S. and their institutions. The other authors declare no competing interests.

Additional information

Supplementary information The online version contains supplementary material available at <https://doi.org/10.1038/s41929-025-01301-0>.

Correspondence and requests for materials should be addressed to Yang Hou, David Sinton or Edward H. Sargent.

Peer review information *Nature Catalysis* thanks Guiyan Zang and the other, anonymous, reviewer(s) for their contribution to the peer review of this work.

Reprints and permissions information is available at www.nature.com/reprints.

Publisher’s note Springer Nature remains neutral with regard to jurisdictional claims in published maps and institutional affiliations.

Springer Nature or its licensor (e.g. a society or other partner) holds exclusive rights to this article under a publishing agreement with the author(s) or other rightsholder(s); author self-archiving of the accepted manuscript version of this article is solely governed by the terms of such publishing agreement and applicable law.

© The Author(s), under exclusive licence to Springer Nature Limited 2025